Spectral Beam Splitting in Compound Parabolic Collector based Photovoltaic Thermal System

Mohit Barthwal[1] and Dibakar Rakshit[1]

[1] Indian Institute of Technology Delhi, New Delhi (India)

Abstract

Spectral beam splitting (SBS) is an approach to eliminate the interdependency between photovoltaic (PV) and photothermal conversion processes in a conventional photovoltaic thermal (PVT) system. Hence, it overcomes the major shortcoming of a traditional PVT system, which is the extraction of low-temperature thermal output as it is limited by the peak operational temperature attained by the PV cells/module. The present work conceptualizes a novel compound parabolic collector (CPC)-based concentrating PVT system utilizing a nanofluid optical filter for SBS. A Monte Carlo Ray Tracing (MCRT) based optical analysis of the devised system is carried out to determine the incident heat flux. Further, the cell temperature associated with the incident flux is determined through a quasi-dynamic thermal analysis. The developed optical and thermal models are verified against the experimental and numerical findings. The devised model emphasized the effectiveness of the nanofluid optical filter by transferring the solar rays within the spectral response range to the PV array while absorbing the rest of the spectrum. The maximum array temperature is recorded to reach as high as 375 K without splitting. However, when employing the SBS approach, this equivalent temperature is retained at 328 K. Hence, the cell temperature is sustained near the standard test temperature via splitting, with no passive or active cooling. Moreover, the maximum cumulative temperature rise is observed to be 58.76 K and 71.88 K for deionized water and ZnO nanofluid, respectively.

Keywords: PVT, Spectral splitting, Compound parabolic collector, MCRT, Nanofluid

1 Introduction

The solar spectrum (250-3000 nm) includes ultraviolet (250-380 nm), visible (380-740 nm), and infrared (740-2500 nm) energy (fig. 1 (b)). However, a photovoltaic (PV) cell operates in a specific spectral response range (SRR) depending on the semiconductor material's bandgap. Most of the solar spectrum up to 1109 nm is converted into valuable electrical energy by c-Si PV cells, while the rest is dissipated as heat, which is called thermalization (Polman and Atwater, 2012). A 1°C increase in the cell temperature reduces the electrical efficiency by 0.4-0.6% (Chander et al., 2015; Kalogirou and Tripanagnostopoulos, 2006). A PVT system prevents any loss of electrical efficiency by cooling the cells while also harnessing a thermal output for various real-world applications (Sathe and Dhoble, 2017).

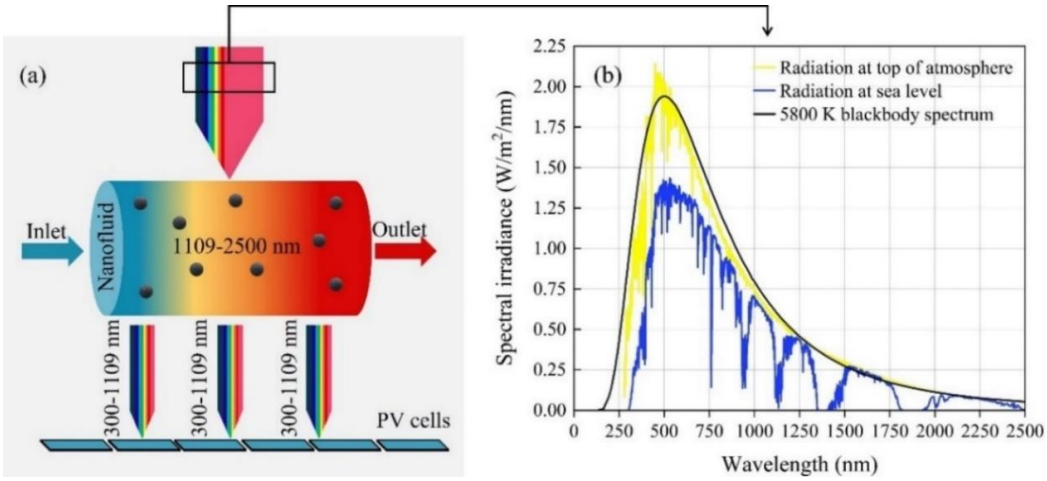

Fig. 1: (a) Concept of solar spectral beam splitting via nanofluid optical filter, and (b) AM1.5 solar spectrum.

Selection and/or peer review under responsibility of Scientific Committee
doi:10.18086/eurosun.2022.12.01 Available at http://proceedings.ises.org

The highest operating temperature of the PV cells/module limits the extraction of high-temperature thermal output (Luo et al., 2020). The cooling fluid can reach 30-45°C (Barthwal and Rakshit, 2021). This low-grade heat output is appropriate only for domestic purposes. The spectral beam splitting (SBS) technique eliminates the dependencies between photovoltaic and photothermal conversions in a PVT system (Fernandes and Schaefer, 2021), allowing for a high-temperature thermal output and improving photovoltaic efficiency. SBS-based PVT divides the solar spectrum into portions based on the PV cell's bandgap cut-off wavelength. Only photons with wavelength (and energy) in the PV semiconductor material's spectral response range are used to generate electrical output to minimize undesirable thermalization.

The SBS can be realized using an optical filter for splitting the wavelengths. It is classified based on the optical filter employed. A thin nanofilm can be utilized to reflect the SRR to the PV array while transmitting the rest to a heat transfer fluid (HTF). Another way is to employ a nanofluid optical filter to absorb the non-SSR wavelengths and transmit the rest to the PV cells (fig. 1 (a)). Using a nanofilm has the drawback of high optical losses due to reflection. Moreover, synthesizing nanofilm is a complex process. On the other hand, a nanofluid optical filter is easier to synthesize and has a volumetric effect in harnessing thermal energy. Also, it is easier to regulate the heat-to-electricity ratio based on the application requirements with varying the nanoparticle concentration of the nanofluid. By employing a Fresnel lens-based CPVT system, (An et al., 2016) used Cu_9S_5 in oleylamine as a nanofluid optical filter. Compared to a typical arrangement with no optical filter, the electrical efficiency of the PV cells was increased by roughly 18% with the assistance of a nanofluid optical filter. A high temperature (100°C) thermal output was also recovered from the CPVT system. (Meraje et al., 2022) also used a nanofluid optical filter to examine the Fresnel lens-based CPVT system. A ZnO nanofluid was synthesized using water-ethylene glycol as the base fluid and visually tested for the SBS. The study suggested ZnO nanofluid for the SBS.

The literature review suggests that the SBS capabilities are investigated for a high concentration solar field-based PVT system. However, an SBS-coupled compound parabolic concentrator (CPC) has not been explored in the literature. The CPC has sparked a lot of interest in solar thermal applications. Yet, no substantial commercial development has occurred. The same is applicable for effectively implementing the SBS technique. Moreover, in order to enable applications operating at low to medium temperatures, it is crucial to investigate the development of a collector with a low concentration ratio. Furthermore, the use of CPC provides the advantage of seasonal tracking, which simplifies the PVT operation. The present work proposes a low concentration CPC-based PVT system with SBS capabilities. A c-Si PV cell with a cut-off wavelength of 1109 nm (corresponding to a 1.12 eV bandgap) is considered. PV cells have an SRR between 300 nm and the semiconductor material's cut-off wavelength (1109 nm). The proposed system's utility is evaluated using an opto-thermal analysis for the location of New Delhi, India.

2 Methodology

2.1. Physical model

Fig. 2 shows the physical model of the proposed system. The CPVT system consists of a CPC collector (fig. 2 (a)), the geometry of which is made from the profiles of two intersecting parabolas (fig. 2 (c)). A collector with a concentration ratio (CR) of 2.8 is truncated to a CR of 2.3 (tab. 1). A PV array consisting of 8 series-connected cells is placed at the absorber/detector (fig. 2 (b)). Borosilicate glass tubes containing nanofluid (as the optical filter) are placed over the PV array to absorb the infrared radiation and transmit the visible spectrum. The spectral transmissivity (τ_λ) and absorptivity (α_λ) of an ideal nanofluid optical filter is given by eq. 1 and 2, respectively. And tab. 2 describes the optical properties of all the components.

$$\tau_\lambda = \begin{cases} 1, & 380\ \text{nm} < \lambda \leq 1100\ \text{nm} \\ 0, & \lambda > 1100\ \text{nm} \end{cases} \quad \text{(eq. 1)}$$

$$\alpha_\lambda = \begin{cases} 0, & 380\ \text{nm} < \lambda \leq 1100\ \text{nm} \\ 1, & \lambda > 1100\ \text{nm} \end{cases} \quad \text{(eq. 2)}$$

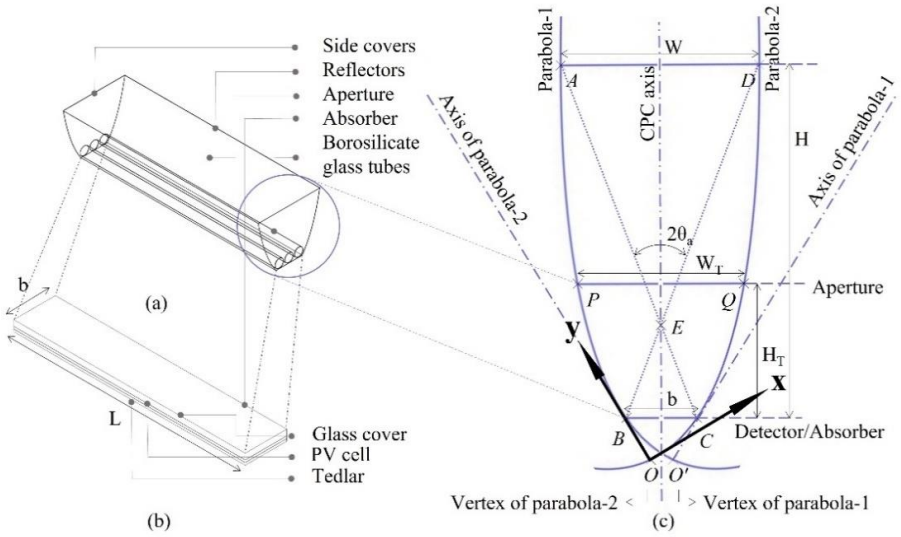

Fig. 2: Physical model of (a) devised spectral beam splitting based concentrating photovoltaic thermal collector, (b) PV array, and (c) geometrical configuration of the compound parabolic concentrator.

Tab. 1: Physical parameters of original and truncated compound parabolic collector (CPC).

Parameter	Original CPC		Truncated CPC	
Acceptance angle (°)	$2\Theta_a$	41.85	$2\Theta_a$	82.96
Concentration ratio (-)	C	2.80	C	2.34
Aperture width (mm)	W	375.20	W_T	314.50
Absorber width (mm)	b	134.00	b	134.00
Collector height (mm)	H	665.87	H_T	253.00
Collector length (mm)	L	1000.00	L	1000.00
Glass tube inner diameter (mm)	D_i	42.60	D_i	42.60
Glass tube outer diameter (mm)	D_o	44.60	D_o	44.60
Pitch (mm)	P	50.00	P	50.00

Tab. 2: Optical properties of concentrating photovoltaic thermal collector components (Parthiban et al., 2022; Zhou et al., 2015).

Component	Material	Thickness (mm)	Absorptivity (α)	Reflectivity	Transmissivity (τ)	Emissivity (ε)
Glazing	Acrylic glass	1.5	0.03	0.02	0.95	0.93
Reflector	Aluminium	1	0.05	0.92	0.03	-
Glass cover	Glass	1.5	0.03	0.02	0.95	0.93
PV cell	-	0.3	0.88	0.12	-	-

2.2. Simulation procedure

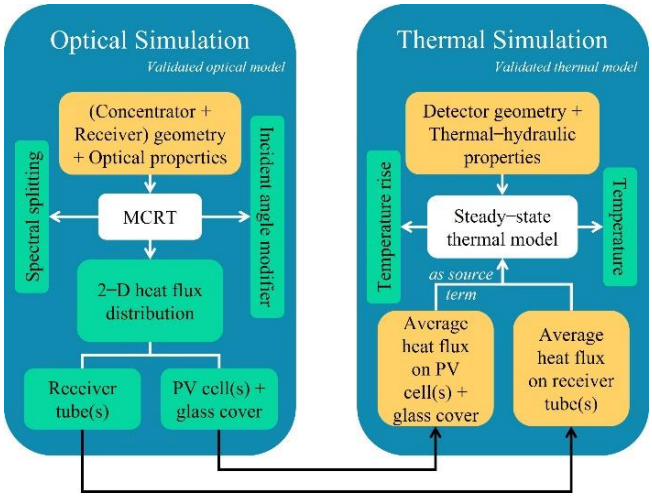

Fig. 3: Simulation methodology workflow for coupled opto-thermal analysis.

The optical simulation is carried out using the MCRT approach (Shadmehri et al., 2018). The incidence angle (Θ_i) of the rays is affected by the orientation, location, surface slope, and time of day (Barthwal and Rakshit, 2021). It is estimated for the months of January and June in New Delhi, India. The concentration and receiver geometry with optical properties are fed to the model to generate a 2-D non-uniform heat flux distribution on PV cell(s), glass cover, and nanofluid tubes. The incoming ray is traced to check if it strikes the reflector, nanofluid, and detector (PV array) or if it is overflown. If the wavelength of this incoming ray is not within the spectral response range, it is absorbed; otherwise, it is transmitted to the detector. Finally, the heat flux of the transmitted, absorbed, and overflown rays is calculated. The resultant heat flux distribution is fed to a steady-state thermal model along with detector/tube geometry and thermal−hydraulic properties to obtain the temperature distribution on the PV array. Fig. 3 shows the adopted methodology workflow.

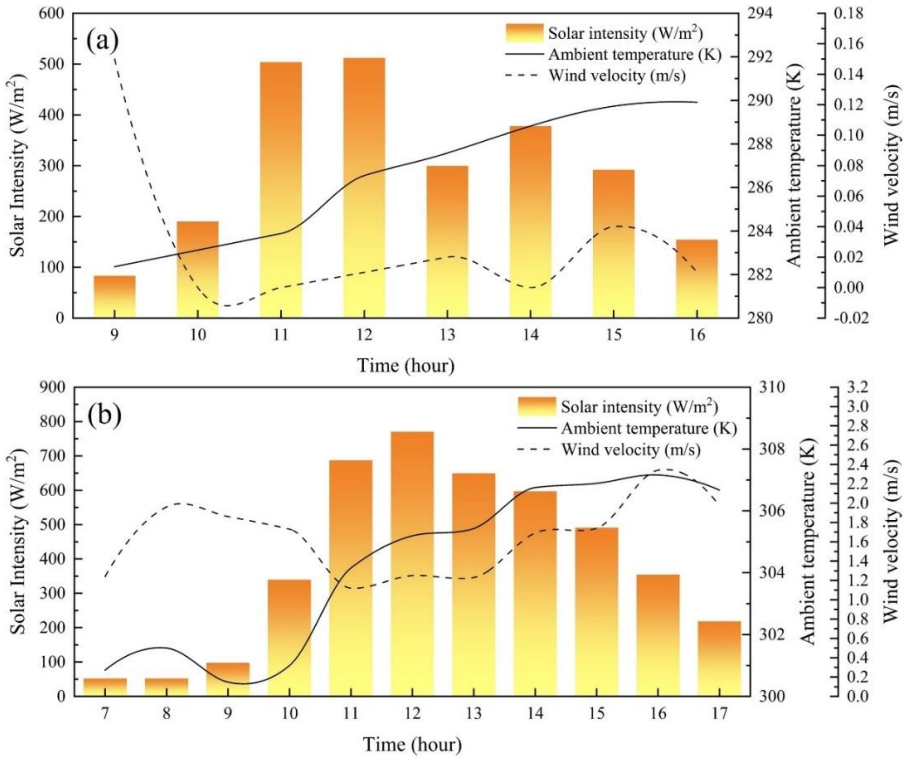

Fig. 4: Graphical representation of average climatic data for the month of (a) January, and (b) June, recorded in real-time via an in-house weather station at New Delhi (28.61°N, 77.20°E).

Because the PV array and nanofluid tube units are not considered to be thermally coupled in the current physical model, the PV array and glass tube units are analyzed separately. The developed model has been evaluated on real-time weather data (fig. 4) recorded by an in-house weather station (fig. 5) in New Delhi, India. The thermo-physical properties of the system components are listed in the tab. 3. The heat generation term ($\dot{Q}$) in eq. 3 is supplied as internal volumetric heat generation at the cell ($\dot{Q}_{cell}$) and glass cover ($\dot{Q}_g$), which are given by eqs. 4 and 5, respectively. Where G denotes the concentrated heat flux at the absorber/detector. And α_{cell}, η_{cell}, and t_{cell} denote the cell's absorptivity, reference efficiency, and thickness, respectively. Similarly, α_g, τ_g, and t_g denote the glass cover's absorptivity, transmissivity, and thickness, respectively. Fig. 6 represents the imposed boundary conditions in the simulation procedure. Cell ($\dot{Q}_{cell}$) and glass cover ($\dot{Q}_g$) heat generation is provided at the cell unit (fig. 6 (a)) along with ascribed convective and radiative heat losses determined through eqs. 6 and 8, respectively. The corresponding convective/wind (h_w) and radiative (h_r) heat transfer coefficients are quantified using eqs. 7 and 9, respectively. Where, v_w and T_{sky} denotes the wind velocity and sky temperature, respectively.

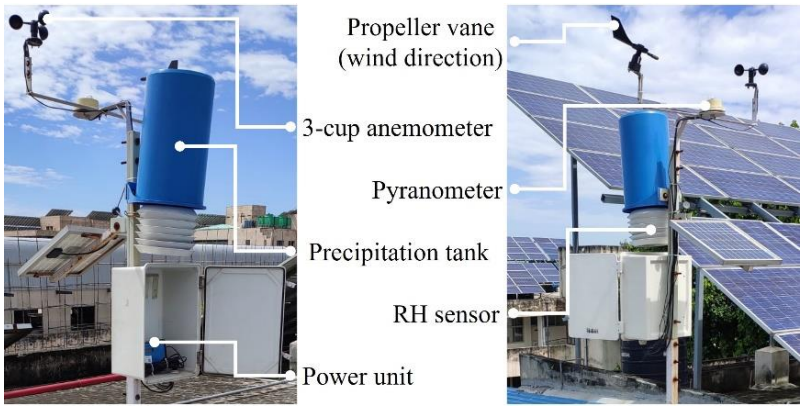

Fig. 5: Weather station for recording the climatic data.

Tab. 3: Thermo-physical properties of concentrating photovoltaic thermal collector components (Baig et al., 2018; Meraje et al., 2022).

Component	Thickness (mm)	Thermal conductivity (W m^{-1} K^{-1})	Density (kg m^{-3})	Specific heat capacity (J kg^{-1} K^{-1})	Viscosity (kg m^{-1} s^{-1})
Glass cover	1.5	1	3000	500	-
Cell	0.3	148	2330	677	-
Tedlar	0.3	0.15	1200	1250	-
DI water	-	0.606	997	4220	8.90 x 10^{-4}
ZnO nanofluid	-	0.376	1057.38	3316.08	2.0122 x 10^{-3}

$$\frac{\partial}{\partial x_j}\left(k\frac{\partial T}{\partial x_j}\right) + \dot{Q} = 0 \qquad \text{(eq. 3)}$$

$$\dot{Q}_{cell} = \frac{G\,\tau_g\,\alpha_{cell}(1-\eta_{cell})}{t_{cell}} \qquad \text{(eq. 4)}$$

$$\dot{Q}_g = \frac{G\,\alpha_g}{t_g} \quad \text{(eq. 5)}$$

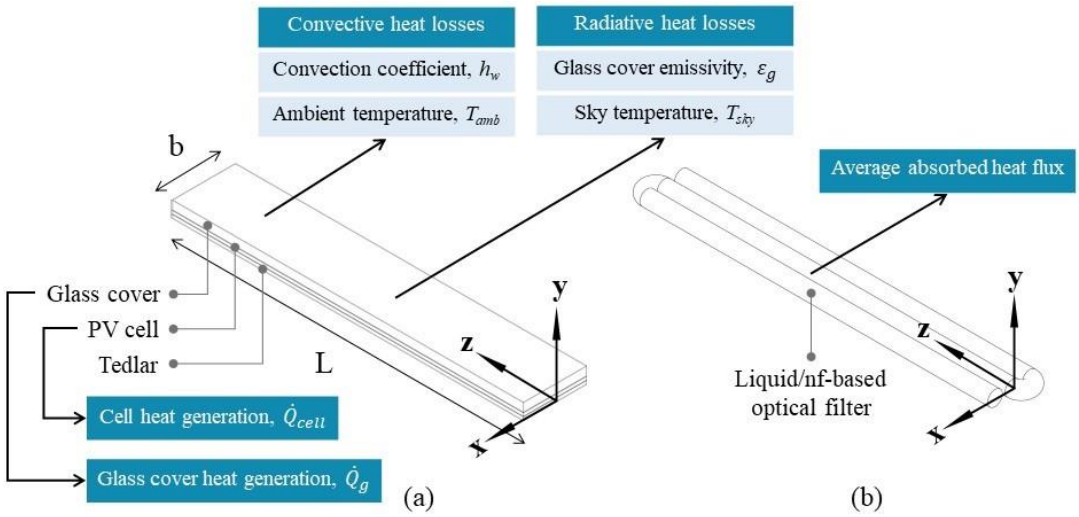

Fig. 6: Boundary conditions imposed at the (a) PV array, and (b) glass tube units.

$$Q_{c,losses} = h_w\left(T_g - T_{amb}\right) \quad \text{(eq. 6)}$$

$$h_w = 5.82 + 4.07\,v_w \quad \text{(eq. 7)}$$

$$Q_{r,losses} = h_r\left(T_g - T_{sky}\right) \quad \text{(eq. 8)}$$

$$h_r = \sigma\,\varepsilon_g\left(T_g^2 + T_{sky}^2\right)\left(T_g + T_{sky}\right) \quad \text{(eq. 9)}$$

The nanofluid in the tube is kept stationary, similar to in (An et al., 2016). For numerical modeling, a negligibly small mass flow rate (5×10^{-4} kg/s) is specified at the tube inlet, along with the hourly ambient temperature recorded by the weather station. At the nanofluid surface, the average absorbed heat flux boundary condition is employed (fig. 6 (b)). Eqs. 10, 11, and 12 give the continuity, momentum, and energy equations for the examined 3-D, steady, laminar flow in the borosilicate glass tube (Liang et al., 2019).

$$\frac{\partial}{\partial x_j}(\rho\,u_i) = 0 \quad \text{(eq. 10)}$$

$$\frac{\partial}{\partial x_j}(\rho\,u_i u_j) = -\frac{\partial p}{\partial x_j} + \frac{\partial}{\partial x_j}\left[\mu\left(\frac{\partial u_i}{\partial x_j} + \frac{\partial u_j}{\partial x_j}\right)\right] + \rho g_i \quad \text{(eq. 11)}$$

$$\frac{\partial}{\partial x_j}(\rho\,u_j C_p\,T) = \frac{\partial}{\partial x_j}\left(k\frac{\partial T}{\partial x_j}\right) \quad \text{(eq. 12)}$$

The computational mesh is generated using Ansys ICEM CFD. A grid-independence study is conducted separately for the PV array and glass tube units to make the solution free from the grid size with respect to cell (T_{cell}) and nanofluid temperature (T_{nf}), respectively (tab. 4). Eq. 13 calculates the percentage error (E_n) corresponding to the number of elements (n) based on the associated temperature value (T_i) versus the next subsequent temperature value (T_{i+1}). Finally, 21708000 and 676494 number of elements are considered for PV array and glass tube units, respectively, for further analysis. The pressure-velocity coupling is realized using the SIMPLE algorithm, and

second-order upwind discretization is employed. The convergence conditions for continuity and momentum are chosen to be < 10^{-3}, and that for energy be < 10^{-6}.

$$E_n = \left|\frac{T_i - T_{i+1}}{T_i}\right| \quad \text{(eq. 13)}$$

Tab. 4: Grid independence analysis for PV array and glass tube units for the unglazed collector.

PV array unit			Glass tube unit		
Number of elements	**T_{cell} (K)**	**E_n**	**Number of elements**	**T_{nf} (K)**	**E_n**
9648000	362.9242	0.30	44608	297.913	0.114
14472000	361.8242	0.22	83640	297.573	0.081
21708000	361.0177	0.002	210048	297.331	0.067
29547000	361.009	0.002	676494	297.131	0.037
36662400	361.001	-	1073034	297.019	0.037
-	-	-	1573200	297.910	-

3 Results and discussion

3.1. Optical analysis

The objective of the optical investigation is to determine the average heat flux received by the photovoltaic cell and the borosilicate glass tube units. The analysis has been carried out on the collector that is oriented east to west, and real-time January and June meteorological data have been utilized.

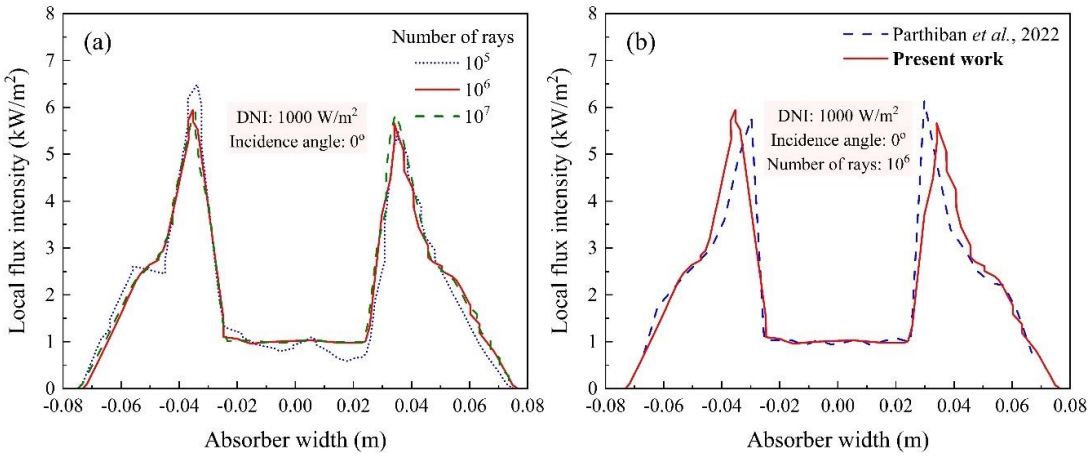

Fig. 7: (a) Ray independence study, (b) Validation of flux intensity on absorber/PV array width for present optical analysis against that by (Parthiban et al., 2022).

The optical model has been validated by the results of (Parthiban et al., 2022) (fig. 7). The reference study utilized a truncated 2.3 CR CPC as in the present work. Tracing fewer rays does not adequately represent the flux intensity at the detector. However, a greater number of rays increases the computing cost of the ray-tracing operation. A ray-independence test is performed to ensure that the local flux intensity (and hence the average flux intensity) at the absorber/detector does not fluctuate with the number of rays traced. The test is carried out with 10^5 to 10^7 rays.

Fig. 7 (a) depicts no reasonable variation in local flux intensity for 10^6 and 10^7 rays. Hence, 10^6 rays are used in further analysis. Also, fig. 7 (b) shows a reasonable agreement of local flux intensity between the present optical model and the reference study.

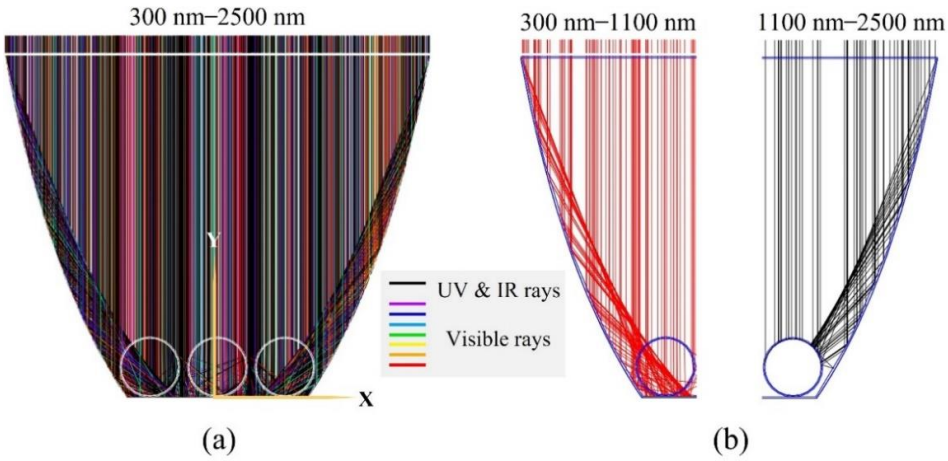

Fig. 8: (a) Traced solar spectrum, and (b) wavelength-sorted traced-rays in the devised collector (only 5% starting rays are shown for better visualization)

The rays traced on the 16th of January 2022 at solar noon (1200 hours) are depicted in fig. 8. These rays represent various wavelengths from the solar spectrum (fig. 8 (a)). In order to facilitate better viewing, only 5% of the initial rays are shown. The spectral beam splitting (SBS) process is observed in operation where rays with wavelengths within the spectrum response range (300–1100 nm) are passed through the photovoltaic array while the remaining wavelengths are absorbed by the nanofluid optical filter (fig. 8 (b)). The central part of the array has to have a uniform flux distribution since the incoming rays do not get deflected by the reflector and strike straight on the absorber/detector. On the other hand, the rays that interact with the reflector are reflected near the detector's edges. As a result, a maximum heat influx will be between the central part and the edges of the absorber/detector.

The incident angle modifier (IAM) is a significant optical analysis index. It represents the decrease in irradiance that reaches the PV cell's surface compared to normal incidence. It is obtained using a basic air-glazing model with one air-glass contact (fig. 9 inset) via eq. 14 (Sjerps-Koomen et al., 1996). The transmission-absorptance ($\tau\,\alpha$) depends on the extinction coefficient (K_e) and the thickness (t) of the glazing for incidence (Θ_i) and refraction (Θ_r) angle duos (eq. 15). Also, Snell's law (eq. 16) is used to quantify refraction angles for different ray incidents. Fig. 9 depicts the variations of IAM as a function of incidence angle. The modifier drops as the ray incidence angle rises because the first (primary) reflection becomes more significant at greater incidence angles. When sun rays enter an angle, these reflection (cosine) losses are responsible for the lower transmission of sun rays through the glass front of a solar cell/module.

$$\mathrm{IAM}(\Theta_i) = \frac{\tau\,\alpha\,(\Theta_i)}{\tau\,\alpha\,(0)} \qquad \text{(eq. 14)}$$

$$\tau\,\alpha\,(\Theta_i) = \exp\left(\frac{-K_e t}{\cos\Theta_r}\right)\left[1 - \frac{1}{2}\left\{\frac{sin^2(\Theta_r - \Theta_i)}{sin^2(\Theta_r + \Theta_i)} + \frac{tan^2(\Theta_r - \Theta_i)}{tan^2(\Theta_r + \Theta_i)}\right\}\right] \qquad \text{(eq. 15)}$$

$$\frac{\Theta_i}{\Theta_r} = \frac{n_g}{n_{air}} \qquad \text{(eq. 16)}$$

The incidence angle modifier is also interpreted in terms of the system's optical efficiency. A greater IAM value corresponds to greater optical efficiency. As the incidence angle of the entering rays rises, the cosine losses resulting from reflection become more pronounced. Consequently, similar to IAM, the optical efficiency follows a declining trend as the incidence angle increases.

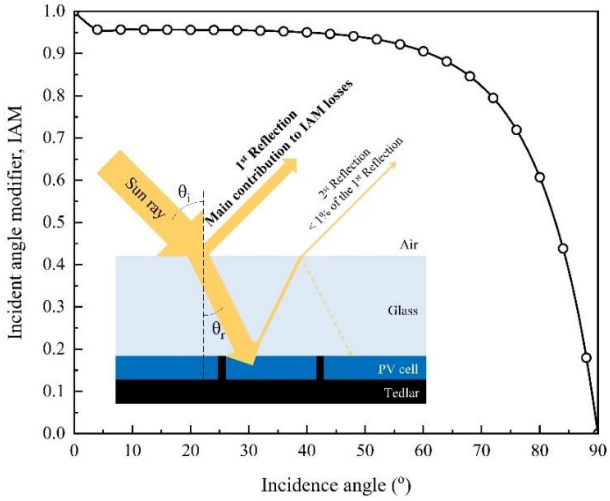

Fig. 9: Variation of incident angle modifier (IAM) with ray incidence angle. (Inset) IAM losses in one air-glass interface model.

3.2. Thermal analysis

The thermal simulation involves the individual analysis of the PV array unit and the nanofluid, as no thermal connection is assumed between the glass tube unit and the PV array. The results of the thermal analysis include validation results with the experimental findings as well as the results of spectral beam splitting in terms of cell temperature and optical filter temperature rise.

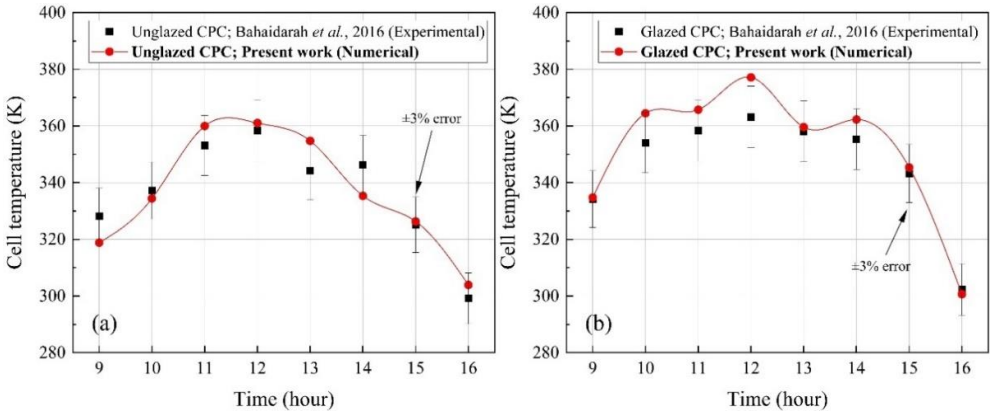

Fig. 10: Validation of temporal cell temperature for (a) unglazed, and (b) glazed collector against the experimental work of (Bahaidarah et al., 2016).

The computed cell temperature is compared to the experimental observations of (Bahaidarah et al., 2016) for both unglazed and glazed collectors to verify the current thermal model. Fig. 10 depicts the temporal variation of cell temperature. At solar noon, the highest average cell temperature is 361 K for the unglazed system and 377 K for the glazed system. When comparing the current thermal model to the experimental results, a maximum of 3% deviation in cell temperature is recorded, validating the thermal simulation approach employed. Another inference can be made in terms of the potential for cooling in concentrating PV cells. The PV cells with a concentrator ought to perform better as compared to the cells without utilizing any concentrator due to the availability of much higher incident heat flux. However, the thermalization limits the potential of the CPV system, and hence a thermal management effort is required to prevent any high temperatures. Without utilizing any passive or active cooling strategy, deionized water and ZnO nanofluids are employed as optical filters for this purpose.

Fig. 11 shows the variation of cell temperature with the time in the day for the winter (January) and summer (June) months. It is observed that the average cell temperature in a conventional CPV system can be as high as 360 K and 375 K for the months of January and June, respectively. However, the cell temperature is maintained near

standard test condition (STC) temperature (298 K) in the proposed nanofluid filter-based system.

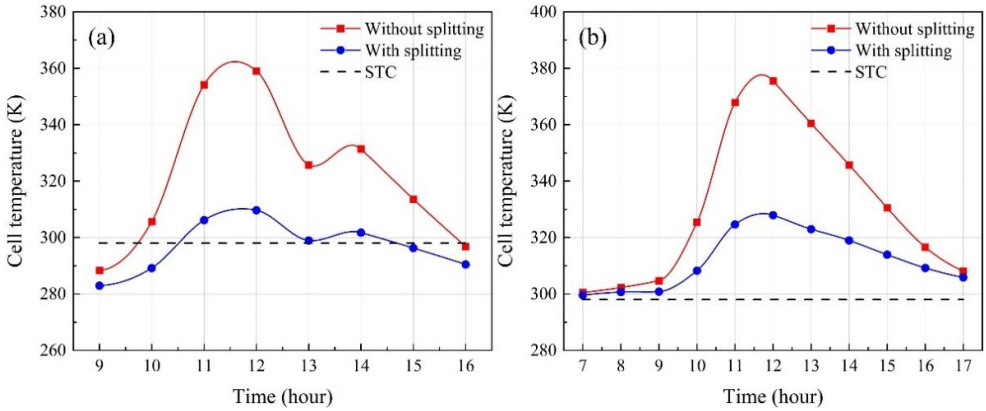

Fig. 11: Temporal variation of average cell temperature for the month of (a) January, and (b) June for the systems placed in New Delhi (28.61°N, 77.20°E).

The temperature rise of the liquid/nanofluid optical filter is also determined. The absorbed heat flux is determined using the optical simulation (fig. 3). Section 2.2 describes the simulation process. Deionized water and ZnO nanofluid (500 ppm ZnO nanoparticles in 50-50% water-ethylene glycol solution) are simulated as the optical filter. Tab. 3 lists the thermophysical characteristics of DI water and ZnO nanofluid. The cumulative temperature rise of the optical filter over time can be seen in fig. 12. The greatest cumulative temperature rise of DI water and ZnO nanofluid at 1600 hours in January is 35.62 K and 43.59 K, respectively. However, during the month of June, DI water and ZnO nanofluid had temperatures of 58.76 K and 71.88 K, respectively.

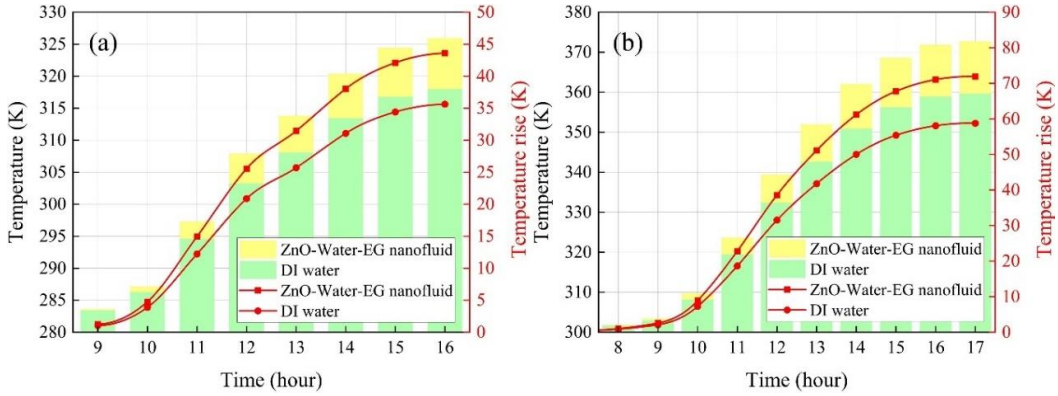

Fig. 12: Temporal variation of cumulative temperature rise of optical filters for the month of (a) January, and (b) June.

4 Conclusions

The opto-thermal analysis of a proposed novel spectral beam splitting powered compound parabolic collector-based photovoltaic thermal system is carried out. Monte Carlo ray-tracing is utilized to observe the prowess of nanofluid-based solar splitting for the cogeneration of electricity and thermal output. Moreover, a finite volume-based solver is utilized for quantifying the thermal output from the devised system. The developed opto-thermal framework is validated with respect to local flux intensity and cell temperature, justifying the methodology employed. The following main findings are summarized for the present work:

- Without resorting to active and/or passive cooling methods, the SBS approach aided in maintaining a cell temperature comparable to the STC temperature.
- The maximum array temperatures of 360 K and 375 K were observed for January and June, respectively, without the SBS employment. With the SBS technique, however, these equivalence temperatures were 310 K and 328 K, respectively.

- DI water and ZnO nanofluid observed the maximum cumulative temperature increases of 35.62 K and 43.59 K, respectively, in January. In contrast, the temperatures of DI water and ZnO nanofluid in the month of June were 58.76 K and 71.88 K, respectively.

Multiple potential intervention avenues have been identified in the current study for use in future investigations. To get a more consistent heat flux distribution, the number of quartz tubes positioned above the PV array (or the number of passes) can be adjusted. Moreover, the heat-to-electricity ratio from the designed PVT collector may be modified by varying the pitch of the tubes. In addition, thermal losses may be avoided by utilizing a concentric glass tube with a vacuum in between.

Acknowledgments

The authors thank HPC facility at IIT Delhi for computational resources. The first author would like to thank the Science and Engineering Research Board (SERB), Government of India, and IIT-Delhi for providing the necessary travel assistance-Grant numbers-ITS/2022/002055, and IITD/PGSR/2022/67221, respectively.

References

An, W., Wu, J., Zhu, T., Zhu, Q., 2016. Experimental investigation of a concentrating PV/T collector with Cu9S5 nanofluid spectral splitting filter. Appl. Energy 184, 197–206. https://doi.org/https://doi.org/10.1016/j.apenergy.2016.10.004

Bahaidarah, H.M., Gandhidasan, P., Baloch, A.A.B., Tanweer, B., Mahmood, M., 2016. A comparative study on the effect of glazing and cooling for compound parabolic concentrator PV systems – Experimental and analytical investigations. Energy Convers. Manag. 129, 227–239. https://doi.org/https://doi.org/10.1016/j.enconman.2016.10.028

Baig, H., Jani, R., Markam, B.K., Maiti, S., Mallick, T.K., 2018. Modelling and experimental analysis of a seasonally tracked V-trough PV/T system in India. Sol. Energy 170, 618–632. https://doi.org/https://doi.org/10.1016/j.solener.2018.06.018

Barthwal, M., Rakshit, D., 2021. Artificial neural network coupled building-integrated photovoltaic thermal system for indian montane climate. Energy Convers. Manag. 244, 114488. https://doi.org/https://doi.org/10.1016/j.enconman.2021.114488

Chander, S., Purohit, A., Sharma, A., Arvind, Nehra, S.P., Dhaka, M.S., 2015. A study on photovoltaic parameters of mono-crystalline silicon solar cell with cell temperature. Energy Reports 1, 104–109. https://doi.org/10.1016/j.egyr.2015.03.004

Fernandes, M.R., Schaefer, L.A., 2021. Multiparticle nanofluid optimization for spectral-splitting energy harvesting. Renew. Energy 173, 849–860. https://doi.org/https://doi.org/10.1016/j.renene.2021.02.116

Kalogirou, S.A., Tripanagnostopoulos, Y., 2006. Hybrid PV/T solar systems for domestic hot water and electricity production. Energy Convers. Manag. 47, 3368–3382. https://doi.org/https://doi.org/10.1016/j.enconman.2006.01.012

Liang, Y., Liu, P., Zheng, N., Shan, F., Liu, Z., Liu, W., 2019. Numerical investigation of heat transfer and flow characteristics of laminar flow in a tube with center-tapered wavy-tape insert. Appl. Therm. Eng. 148, 557–567. https://doi.org/https://doi.org/10.1016/j.applthermaleng.2018.11.090

Luo, K., Ji, J., Xu, L., Li, Z., 2020. Seasonal experimental study of a hybrid photovoltaic-water/air solar wall system. Appl. Therm. Eng. 169, 114853. https://doi.org/https://doi.org/10.1016/j.applthermaleng.2019.114853

Meraje, W.C., Huang, C.C., Barman, J., Huang, C.Y., Kuo, C.F.J., 2022. Design and experimental study of a Fresnel lens-based concentrated photovoltaic thermal system integrated with nanofluid spectral splitter. Energy Convers. Manag. 258, 115455. https://doi.org/https://doi.org/10.1016/j.enconman.2022.115455

Parthiban, A., Mallick, T.K., Reddy, K.S., 2022. Integrated optical-thermal-electrical modeling of compound parabolic concentrator based photovoltaic-thermal system. Energy Convers. Manag. 251, 115009. https://doi.org/https://doi.org/10.1016/j.enconman.2021.115009

Polman, A., Atwater, H.A., 2012. Photonic design principles for ultrahigh-efficiency photovoltaics. Nat. Mater. 11, 174–177. https://doi.org/https://doi.org/10.1038/nmat3263

Sathe, T.M., Dhoble, A.S., 2017. A review on recent advancements in photovoltaic thermal techniques. Renew. Sustain. Energy Rev. 76, 645–672. https://doi.org/https://doi.org/10.1016/j.rser.2017.03.075

Shadmehri, M., Narei, H., Ghasempour, R., Shafii, M.B., 2018. Numerical simulation of a concentrating photovoltaic-thermal solar system combined with thermoelectric modules by coupling Finite Volume and Monte Carlo Ray-Tracing methods. Energy Convers. Manag. 172, 343–356. https://doi.org/https://doi.org/10.1016/j.enconman.2018.07.034

Sjerps-Koomen, E.A., Alsema, E.A., Turkenburg, W.C., 1996. A simple model for PV module reflection losses under field conditions. Sol. Energy 57, 421–432. https://doi.org/https://doi.org/10.1016/S0038-092X(96)00137-5

Zhou, J., Yi, Q., Wang, Y., Ye, Z., 2015. Temperature distribution of photovoltaic module based on finite element simulation. Sol. Energy 111, 97–103. https://doi.org/https://doi.org/10.1016/j.solener.2014.10.040

Nomenclature

List of Acronyms			
CFD	Computational Fluid Dynamics	MCRT	Monte Carlo Ray-Tracing
CPC	Compound Parabolic Collector	PVT	Photovoltaic Thermal
CPVT	Concentrating Photovoltaic Thermal	SBS	Spectral Beam Splitting
CR	Concentration Ratio	SRR	Spectral Response Range
DI	Deionized	STC	Standard Test Condition
HTF	Heat Transfer Fluid	SIMPLE	Semi-Implicit Method for Pressure Linked
IAM	Incident Angle Modifier		Equations
List of Symbols			
C	Concentration ratio (-)	W	Aperture width (m)
C_p	Specific heat capacity (J/kg.K)	$\dot{Q}$	Heat generation (W/m^3)
D	Diameter (m)	b	Absorber width (m)
E	Error (-)	g	Acceleration due to gravity (m/s^2)
G	Solar radiation (W/m^2)	h	Heat transfer coefficient (W/m^2K)
H	Height (m)	n	Number of elements/Refractive index (-)
L	Length (m)	t	Thickness (m)
T	Temperature (K)	u/v	Velocity (m/s)
List of Greek Symbols			
α	Absorptivity (-)	τ	Transmissivity (-)
ε	Emissivity (-)	Θ_a	Half-acceptance angle (°)
ρ	Density (kg/m^3)	Θ_i	Incidence angle (°)
σ	Stefan-Boltzmann constant (W/m^2K^4)	Θ_r	Refraction angle (°)